

## Synthesis and characterizations of Mg-Cu-Co-Dy ferrites and their composites with graphene nanoplatelets (GNP)

M. Akhtar<sup>a</sup>, G. Hussain<sup>b</sup>, M. Yusuf<sup>c</sup>, N. Amin<sup>a</sup>, M. I. Arshad<sup>a,\*</sup>

<sup>a</sup>*Department of Physics, Government College University, Faisalabad, Pakistan 38000.*

<sup>b</sup>*Department of Physics, University of Agriculture, Faisalabad, 38040, Pakistan.*

<sup>c</sup>*Department of Clinical Pharmacy, College of Pharmacy, Taif University, Taif 21944, Saudi Arabia.*

Nanocrystalline spinel ferrite  $Mg_{0.5}Cu_{0.25}Co_{0.25}Fe_{1.97}Dy_{0.03}O_4$  (*MCCD-ferrites*) and their composites with graphene nanoplatelets (GNP = 0.0%, 1.25%, 2.5%, 3.75%, 5%) were prepared by sol-gel technique and sintered at 850 °C for 5 hours. Measurements in the areas of X-ray diffraction, electrical, optical, dielectric and magnetic properties were used to analyze the effects of the inclusion of graphene with ferrite nanoparticles. The crystallite size was determined in the range of 27.62 – 41.46 (nm). The optical bandgap was found in the range of 3.50 eV to 2.88 eV. The dielectric loss was measured between 8 Hz and 8 MHz at room temperature (RT). Magnetic characteristics of the materials are measured and calculated. The magnetic performances of *MCCDF-GNP* Composites nanoparticles are improved with an increase in saturation ( $M_s$ ) magnetization. This material can be utilized for humidity sensors, antennae, and micro memory chips.

(Received April 4, 2022; Accepted July 25, 2022)

Keywords: Composites, Crystalline size, Bandgap, Resistivity, Magnetization

### 1. Introduction

Due to the current day's explosive growth of communications systems and the electronic industries, which generate electromagnetic pollution, the environment, and human health are at risk. It is challenging to create microwave absorbers that are effective in reducing electromagnetic interference (EMI) [1]. Due to the combined effect of their magnetic and dielectric characteristics, they are useful for microwave absorbers. However, because of the large ferrite density, small impedance matching, and low magnetic losses, their capacity to provide electromagnetic defense is limited [2]. Graphene oxide (GO) [3] may help to address these drawbacks. In addition to oxygen-containing functional groups, the honeycomb lattice of monoatomic thin layer graphene oxide also contains  $sp^3$  hybridized tetrahedral bound carbon atoms linked to the basic plane and  $sp^2$  hybridized trigonal bound carbon atoms [3][4][5]. The number of oxygen functional groups generated depends on the kind of preparation and corrosion rate. As a consequence, graphene oxide is a chemical molecule made up of carbon, hydrogen, and oxygen that is not stoichiometric [6]. Hydroxyl (-OH), epoxide (-O-), carbonyl (C=O), and carboxyl (-COOH) are the four main functional groups that may be discovered in GO [8]. The addition of O-functional groups causes Van der Waals inter-sheet forces to be overcome, interfacial space to widen [9], and GO to have a neutral and hydrophilic character. Low population density, large specific surface area, great mechanical strength, and the ability to act as an electromagnetic shield are all characteristics of graphene as well as its oxide [10][9]. To expand the effective bandwidth with more absorbance, graphene oxide's ionic conductivity and larger dielectric loss may be combined with ferrite's susceptibility [7]. As a consequence, microwave impedance matching and attenuation will be enhanced [2]. Many studies have been done to improve the composites absorption capabilities. Graphene oxide (GO), a recently created functional carbon material, is distinguished by its exceptional properties, including an ultra-thin two-dimensional atomic layer thickness, a high

---

\* Corresponding author: mimranarshad@gcu.edu.pk  
<https://doi.org/10.15251/JOR.2022.184.539>

specific surface area, thermal properties, and specific strength [8][9]. As a result, GO may be employed as an appropriate nanocomposites carrier, minimizing agglomeration and enhancing catalytic activity. Boopathi Raja et al. studied those two distinct precipitate agents that were used in a suggested hydrothermal approach to creating  $\text{CuCo}_2\text{O}_4$  nanocomposite, resulting in discontinuous nanoparticles with a diameter of approximately of about 25 nm [10]. Li et al. proposed that the synthesis of a  $\text{CuCo}_2\text{O}_4$  nanocomposite with a microsphere shape using ethanol as the solvent [11]. Sun et al. proposed that they created  $\text{CuCo}_2\text{O}_4/\text{rGO}$  nanoparticles and nanofilms, 2D nanosheets, and 3D rose- and daisy-like nanoflowers in various solvent combinations (ethanol, ethylene glycol, deionized water, methanol, and polyethylene glycol 600) [11]. Ameer et al. [12] studied that the  $\text{CoFe}_2\text{O}_4$  - rGO nanohybrids with extremely low absorption coefficients and tangent loss have been reported. Lower frequency electromagnetic shielding has been shown to be suitable for nanohybrids with reflection losses less than 10 dB at frequencies ranging from 12.2 MHz for pure Co - ferrite nanoparticles to 2.95 GHz for nanomaterials (under 3GHz). Vara et al. [13] stated that mixed Cu-Ni, Co-Mn, and Ni-Zn ferrites generated by co-precipitation as catalysts were studied for their thermal behavior using thermogravimetric methods. Additionally, they noticed that mixing different ferrites decreased the breakdown temperature and transmitted solar, with Co-Mn ferrite exhibiting the highest catalytic activity. The magnetic behavior of  $\text{MgFe}_{2-x}\text{Dy}_x\text{O}_4$  produced using the sol-gel process is influenced by the external phase ( $\text{DyFeO}_3$ ) that appears just above concentration of  $x=0.05$  [12]. Karimi el al. studied that the Saturation magnetization decreases with  $\text{Dy}^{3+}$  substitution in co-precipitated Dy doped  $\text{CoFe}_2\text{O}_4$ , but coercivity increases initially and then lowers [14]. According to Jain et al., increased Dy doping in  $\text{CoFe}_2\text{O}_4$  caused an increase in rod-like shape. The magnetic anisotropy of doped systems is impacted by the fact that magnetic characteristics vary in all directions [19]. However, additional concerns must be addressed, such as the presence of impurity phase beyond a certain doping concentration [20][21], doping-induced shape and magnetic anisotropy [14][18], and the tendency of magnetic behavior with  $\text{Dy}^{3+}$  substitution [18][19]. The aim of this work to investigate the effect of GNP on structure, electrical, optical, dielectric, and magnetic properties of  $\text{Mg}_{0.5}\text{Cu}_{0.25}\text{Co}_{0.25}\text{Fe}_{2-x}\text{Dy}_x\text{O}_4$  /GNP ( $x/\text{GNP}\%=0.0/0.0\%$ ,  $0.03/0.0\%$ ,  $0.03/1.25\%$ ,  $0.03/2.25\%$ ,  $0.03/3.75\%$ ,  $0.03/5\%$ ) ferrite composites (*MCCDF-GNP Composites*).

## 2. Materials and methods

Sol-gel technique was used to the preparation of  $\text{Mg}_{0.5}\text{Cu}_{0.25}\text{Co}_{0.25}\text{Fe}_{2-x}\text{Dy}_x\text{O}_4$  /GNP ( $x/\text{GNP}\%=0.0/0.0\%$ ,  $0.03/0.0\%$ ,  $0.03/1.25\%$ ,  $0.03/2.25\%$ ,  $0.03/3.75\%$ ,  $0.03/5\%$ ) ferrite composites. The materials  $\text{Mg}(\text{NO}_3)_2 \cdot 6\text{H}_2\text{O}$ ,  $\text{Dy}(\text{NO}_3)_3 \cdot 6\text{H}_2\text{O}$ ,  $\text{Cu}(\text{NO}_3)_2 \cdot 3\text{H}_2\text{O}$ ,  $\text{Co}(\text{NO}_3)_2 \cdot 3\text{H}_2\text{O}$ ,  $\text{Fe}_2\text{O}_3 \cdot 9\text{H}_2\text{O}$ , GNP, and citric acid are used. Stoichiometric calculations were utilized to determine which nitrates to employ. Citric acid was also utilized as a combustible. To begin, dissolve the nitrates and citric acid in di ionized water using a 1:1 molar ratio. Individual nitrates and citric acid were dissolved in distilled water using magnetic stirring. After that, all of the solutions were mixed in one beaker to make a homogeneous solution. Dropwise Ammonia Solution was added to the solution to keep the pH at 7. The dry gel was produced at 90-100 °C after the continuous stirring of the solution for about 1 hour. Stirring was stopped when the dry gel was formed, and the gel was only heated until the result was reached, as illustrated in figure 1.



Fig. 1. Prepared ash of MCCDF-GNP Composites.

Then, for half an hour, grinding was done to improve the form of the produced samples. After that, the powder was put in a furnace for sintering at 850 °C for 5 hours. Following that, the powder was pressed in a hydraulic press to make pellets at a pressure of 1500 MPa.

An X-Ray Powder Diffraction (Bruker D8) technique with a Cu k source of wavelength 1.5406 was utilized to confirm the spinel cubic structure with single phase creation of all produced specimens. The XRD diffraction pattern was used to compute the bulk density, x-ray density, porosity, theoretical density, experimental density, lattice constant, crystallite size, d-spacing, strain, dislocation density, and packing fraction. The electrical parameter DC resistivity was estimated using two probe I-V measurement techniques. Using absorption spectra, UV-VIS spectroscopic analysis was utilized to determine the optical bandgap ( $E_g$ ) of each material. A commercial spectrometer called the LABRAM-HR was used to record Raman spectra. A vibrating sample magnetometer (VSM) with a maximum applied magnetic field of around  $\pm 3000$  (Oe) was utilized to assess the magnetic behavior of the fabricated specimen at room temperature (RT).

### 3. Result and Discussion

#### 3.1. X-Ray Diffraction Analysis

Fig 2 Shows the XRD pattern of the *MCCDF-GNP Composites*. The crystalline size, lattice parameter, volume of unit cell, x-ray density and bulk density etc. is find out by using this XRD pattern. The face-centered cubic (FCC) structure for spinel ferrite with  $Fd_{3m}$  space group was validated by comparing the XRD pattern of  $Mg_{0.5}Cu_{0.25}Co_{0.25}Fe_{1.97}Dy_{0.03}O_4$  ferrite sintered at 850 ° C with (Powder Diffraction File, card 21–1152). The (hkl) planes (220), (311), (400), and (511) were given to the diffraction peaks seen at 30.250° , 35.63° , 43.29° , and 57.28° , respectively. Bragg's law was used to compute the interplanar spacing (d):

$$2d_{hkl} \sin\theta = n\lambda \quad (1)$$

with  $n = 1$ ,  $\lambda = 1.5406 \text{ \AA}$  and  $\theta$  are represents (order of diffraction), wavelength of incident  $CuK\alpha$  radiations, and Bragg angle [15]. The d-spacing was discovered to be between 2.5215 and 2.5257.

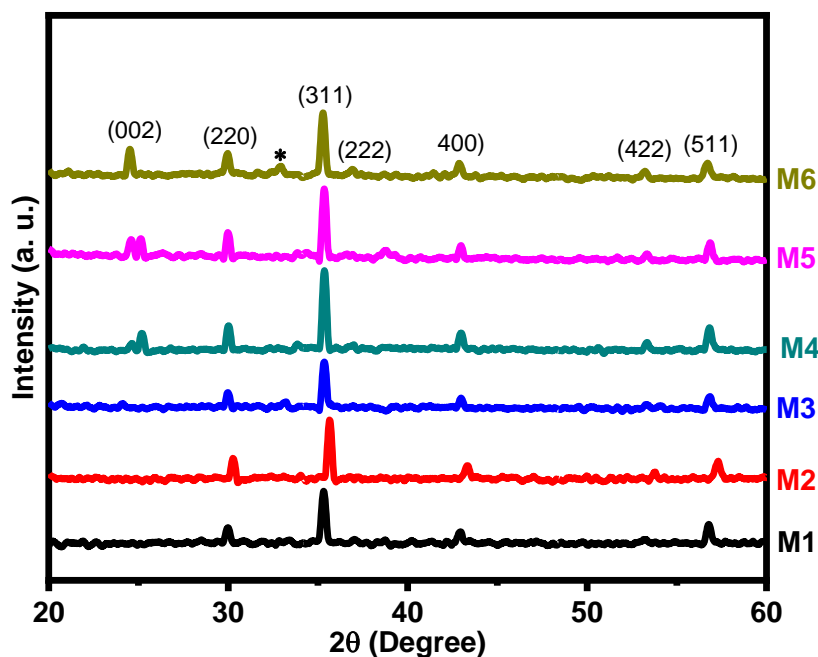


Fig. 2 .XRD pattern of MCCDF-GNP Composites.

In comparison to JCPDS card 01 075 1621, the X-ray diffraction profile of graphene oxide shows a lower intensity of the typical (002) diffraction peak of natural graphite at  $2\theta = 26.60^\circ$

with  $d = 2.5230$  nm. All the characteristic peaks of *MCCDF-GNP* Composites can be seen in the figure 2. The chemical interaction between graphene oxide and ferrite nanoparticles does not occur because graphene oxide has a low inherent crystalline nature [23]. In sample (M6), *MCCD-ferrites* with a higher amount of GO generated a tiny peak at  $26.60^\circ$  for the (002) plane of graphene, which was obscured by high-intensity *MCCD-ferrites* peaks in other composites. This reveals that the formation of *MCCD-ferrites* nanoparticles between GO layers causes shearing and disintegration of stacking layers as well as aggregation in GO sheets [24]. Furthermore, M6 included the secondary phase of  $\text{Fe}_2\text{O}_3$ , which denoted by an asterisk (\*). The existence of  $\text{Fe}_2\text{O}_3$  traces in the iron nitrate employed as a precursor was attributed to this. The following classical formula was used to calculate the lattice parameter ( $\text{\AA}$ ) for each sample using the hkl plane and appropriate d-spacing value [16].

$$a = \frac{\lambda}{2\sin\theta} \sqrt{h^2 + k^2 + l^2} \quad (2)$$

The lattice constant of *MCCD ferrite-GNP composites* (8.41-8.433  $\text{\AA}$ ) are greater than pure MCC-ferrite (8.40  $\text{\AA}$ ) and *MCCD-ferrite* (8.34  $\text{\AA}$ ). The unit cell volume of each sample was calculated by using this relation [18][19]:

$$V_{cell} = a^3 \quad (3)$$

The Unit cell volume parameter of *MCCDF-GNP* Composites was found in the range of 600.29 – 581.40 ( $\text{\AA}^3$ ) as show in table 1. The average crystallite size (D) of (311) peak was calculated by using Scherer's formula [17] [20][21].

$$D = \frac{k\lambda}{\beta_{hkl}\cos\theta} \quad (4)$$

where,  $k = 0.94$ ,  $\lambda = 1.5406$   $\text{\AA}$  and source of (Cu  $K_\alpha$ ), and  $\beta$  are shape factors for cubic crystals and full width at half maximum (FWHM in radians) centered at  $2\theta$  of the highest intense peak (311) [17]. The crystallite size was found in the range of 27 - 41 nm as depicted in Table 1. The addition of GNP to *MCCD-ferrites* causes structural deformation and macrostrain [22]. Similarly equation (5) was used to get the X-ray density

$$d_{x\text{-ray}} = \frac{ZM}{N_A V_c} \quad (5)$$

where  $N_A = 6.022 \times 10^{23} \text{ mol}^{-1}$ , while M indicate the molecular weight of ferrite composite [23].

Table 1 Sample IDs and XRD parameters of MCCDF-GNP Composites

Parameters Sample ID	X/GNP% values	$2\theta$	hkl	Crystalline Size(nm)	Lattice Const ant ( $\text{\AA}$ )	Volume of unit cell ( $\text{\AA}^3$ )	X-Ray Density
M1=Mg-Cu-Co Ferrite	0.00/0.00 %	35.38	311	27.62	8.40	592.93	4.68
M2=Mg-Cu-Co-Dy Ferrite	0.03/0.00 %	35.62	311	41.46	8.34	581.40	4.88
M3= Mg-Cu-Co-Dy Ferrite & GNP 1.25% Composites	0.03/1.25 %	35.33	311	38.67	8.41	595.37	4.77
M4= Mg-Cu-Co-Dy Ferrite & GNP 2.5% Composites	0.03/2.5%	35.42	311	29.50	8.42	590.98	4.74
M5= Mg-Cu-Co-Dy Ferrite & GNP 3.75% Composites	0.03/3.75 %	35.23	311	30.10	8.43	600.29	4.69
M6= Mg-Cu-Co-Dy Ferrite & GNP 5% Composites	0.03/5%	35.24	311	28.99	8.433	599.78	4.75

### 3.2. UV-visible spectroscopy

UV-visible spectroscopy was used to determine the energy band gap ( $E_g$ ) of *MCCDF-GNP composites*. For this purpose, solution of *MCCDF-GNP Composites* was designed by de-ionized water as a solvent. The absorption coefficient ( $\alpha$ ) was determined expending the equation below.

$$\alpha = 2.303 \log(A) / l \quad (6)$$

Here,  $A$  and  $l$  are representing absorbance and the path length of light in which absorbance takes place. Equation (7) shows the relationship between absorbance coefficient ( $\alpha$ ) and optical energy band gap ( $E_g$ ).

$$\alpha h\nu = B (h\nu - E_g)^m \quad (7)$$

Here,  $B$  is constant and  $h\nu$  represents photon energy [33][34]. The optical band gap was determined by plotting the  $(\alpha h\nu)^2$  versus incoming photon energy ( $h\nu$ ). Fig. 3 clearly showed that the band gap reduces as the Dy - GNP proportion increases. The band gap energy of MCD-ferrites-GNP composites was determined to be in the range of 3.50- 2.88 (eV), as shown in fig 3 [24].

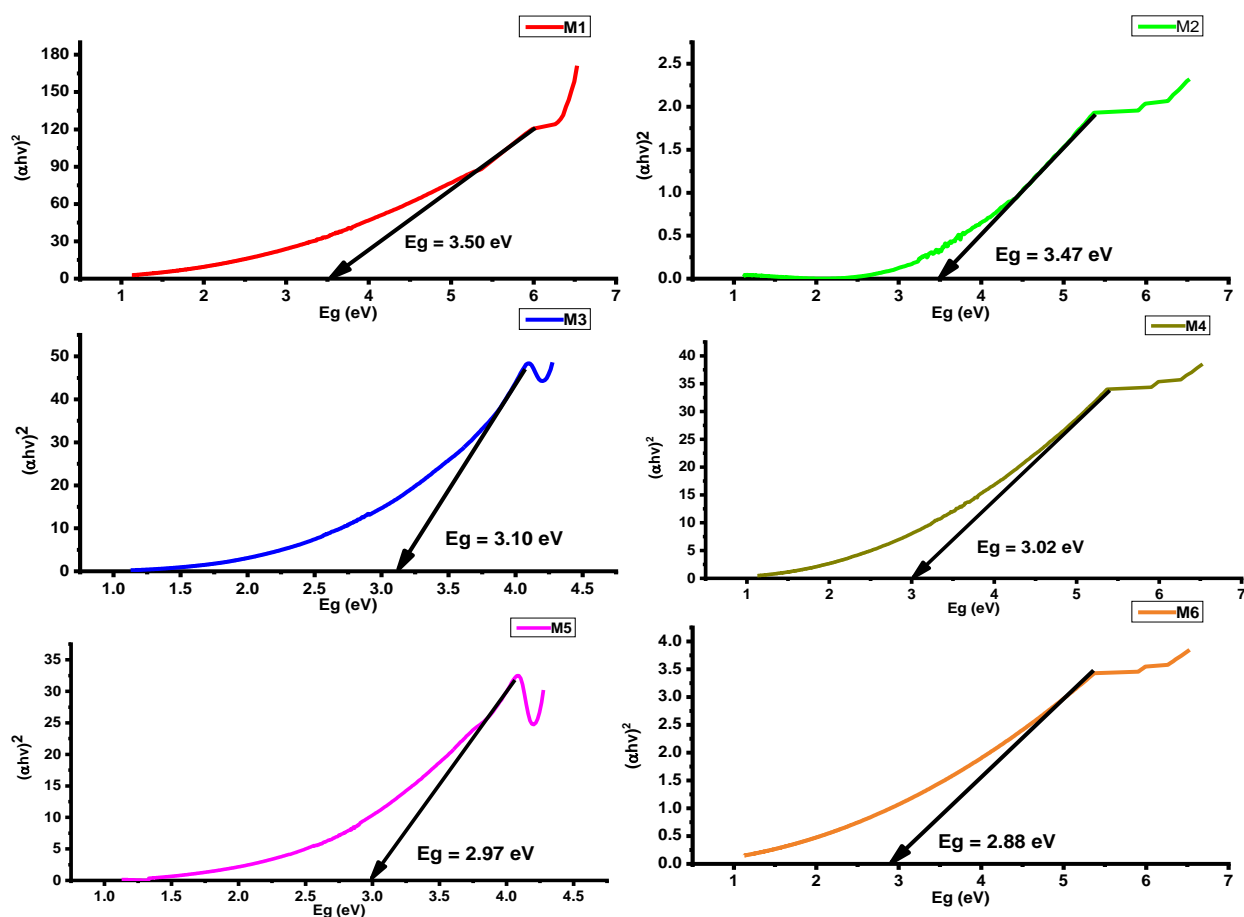


Fig 3 Pattern of UV vis spectroscopy MCCDF-GNP Composites

### 3.3. Current Voltage Analysis

DC resistivity of MCCDF-GNP Composites was determined by the Keithley source meter Model 2401 by using the two probe I-V measuring procedure [25] from temperature between 323-873 K with increments of 50 K. The value of DC resistivity is calculated by using the equation.

$$R = \rho L / A \quad (8)$$

$$\rho = RA / L \quad (9)$$

where, R, L and A are represents resistance, thickness and area of pallet. The graphs of log resistivity verses MCCDF-GNP composites were drawn in below figure 4.

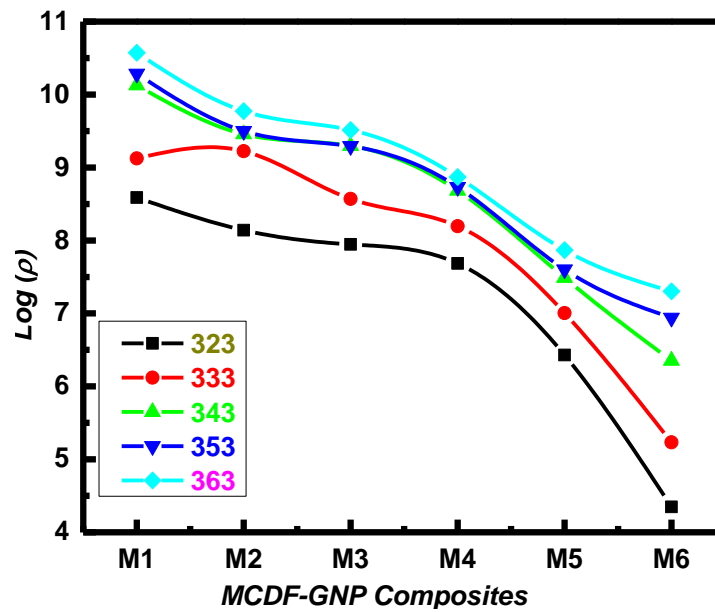


Fig 4: Trend of resistivity due to GNP on MCCDF-GNP composites at different temperatures.

The above graph showed that the resistivity had a decreasing trend of *MCCDF-GNP* composites, this is because of conducting nature of GNP and dysprosium.

### 3.4. Dielectric analysis

Electrical dipoles are produced in the spinel material by the communication of the charged di- and trivalent metal ions. The dielectric behavior of iron oxide is determined by its chemical composition, sintering temperature, metal ion distribution among A and B-sites, and production procedures [36][37]. In figure 5 dielectric losses ( $\tan \delta$ ) were represented as a function of applied frequency from 8 Hz to 8 MHz at room temperature of the *MCCDF-GNP* Composites samples to investigate the influence of GNP variation. As seen in Fig.5, the value of  $\tan \delta$  is greatest at low frequencies and lowest at high frequencies. Because conduction grains are less effective at low frequencies than grains with narrower boundaries, dielectric tangent losses are higher [26].

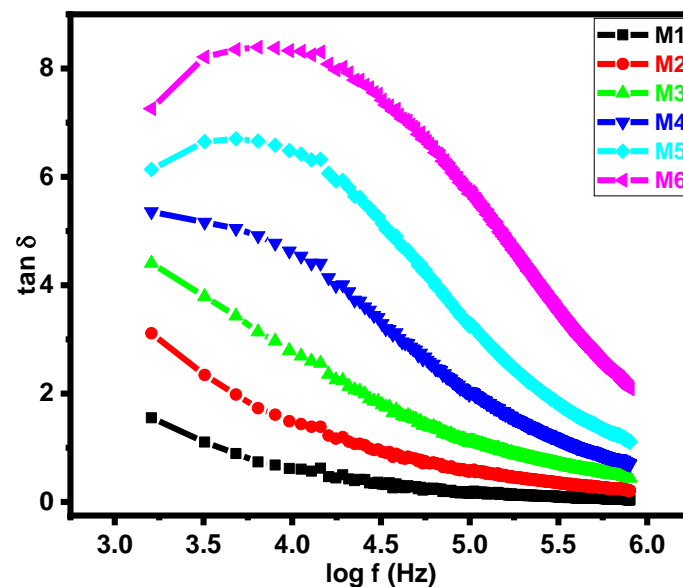


Fig. 5: Tangent loss ( $\tan \delta$ ) variation with frequency of *MCCDF-GNP* composites.

### 3.5. Raman Spectroscopy

The Raman spectrum of *MCCDF-GNP composites* was obtained between 0 and 600  $\text{cm}^{-1}$  and is shown in Fig. 6. It was analyzed to learn more about its vibrational characteristics. Ferrites having a spinel structure and eight formula units per unit cell are classified as Fd-3m. Matching to space group theory, ferrites have the corresponding optical phonon modes at the location of the Brillouin zone: i.e.,

$$\Gamma = A_{1g}(R) + E_g(R) + T_{1g} + 3T_{2g}(R) + 2A_{2u} + 2E_u + 5T_{1u}(IR) + 2T_{2u} \quad [27].$$

The presence of an inversion center in the Centro-symmetrical model vibrational mode for the same vibrational mode. Fig (6) For *MCCDF-GNP ferrite Composites*.  $A_{1g}(R)$ ,  $E_g(R)$ ,  $T_{2g}$ , and five initial active modes have been detected in the Raman spectra (R). A, E, T, and g indicate one-, two-, and three-dimensional representations, respectively, in addition to symmetry to the center of inversion.

Table 2 Room temperature (RT) Raman modes for *MCCDF-GNP ferrite Composites*

Sample ID	$T_{2g}(1)$	$E_g$	$T_{2g}(2)$	$T_{2g}(3)$	$A_{1g}$
	Tetrahedral (A) Site [28]	Octahedral (B) Site [28]	Octahedral (B) Site [28]	Octahedral (B) Site [28]	Tetrahedral (A) Site [28]
M1	147	165.25	241.72	298.63	351.34
M2	150	164.56	242.84	297.94	359.37
M3	152	164.56	241.03	297.67	361.69
M4	151	169.63	242.95	301.09	362.79
M5	164	184.12	242.95	302.32	345.28
M6	153	183.58	243.50	302.32	345.30

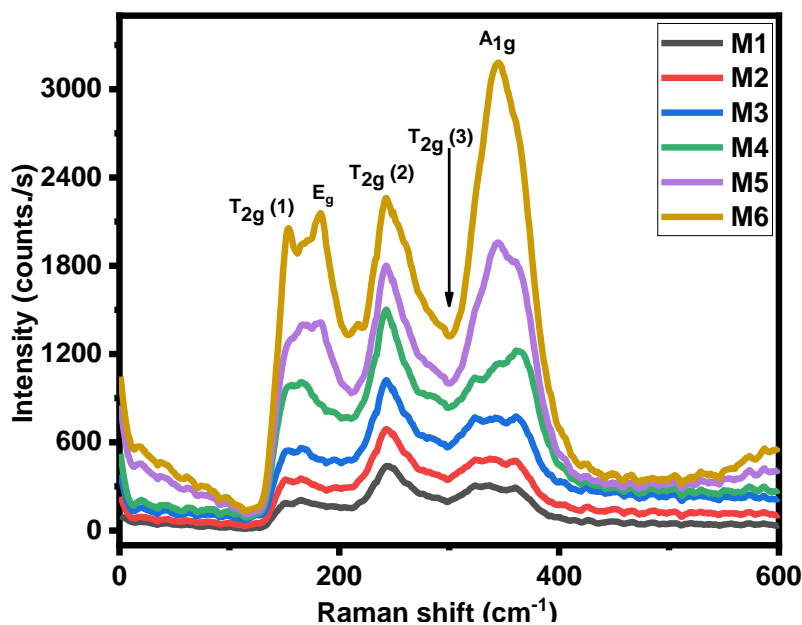


Fig.6 : Raman spectroscopy of *MCCDF-GNP Composites*

The five active modes in spinel cubic structure ferrites correlate to the mobility of oxygen metal ions.  $T_{2g}(3)$  appears at  $302.30 - 297.94 \text{ cm}^{-1}$  and is due to an antisymmetric reaching of Fe and  $O_2$ .  $A_{1g}$  emerges at  $351.34 - 362.28 \text{ cm}^{-1}$  and is attributable to symmetric and asymmetric bending of  $O_2$  to Fe.  $T_{2g}(2)$  appears at  $241.72 - 243.50 \text{ cm}^{-1}$  [40][41].  $E_g$  is unbalanced  $O_2$  bending to Fe that is discovered between  $164.56$  and  $184.13 \text{ cm}^{-1}$ . At  $147.46 - 164.97 \text{ cm}^{-1}$ ,  $T_{2g}(1)$ , which is the symmetric bending of  $O_2$  to Fe, is found. The asymmetric response of the crystal field, as evidenced by vibrating dipoles, causes the peaks to expand. As a result, we believe it supports the concept.

### 3.6. Magnetic Analysis

The magnetic behavior of *MCCDF-GNP* Composites were calculate using vibrating sample magnetometer (VSM) analysis at room temperature with applied field of  $\pm 3000$  (O e). The magnetic hysteresis loops (M-H curves) of *MCCDF-GNP* ferrite Composites were shown in Fig. 7. The addition of GNP and Dy ions to the MCCDF-ferrites system has a substantial effect on the magnetic characteristics. With Dy and GNP ions concentration, magnetization ( $M_s$ ) was found to be in the region of  $(95.00 - 42.71 \text{ emu/g})$  and Initial permeability ( $\mu_i$ ) was determined to be in the range of  $(72.42 - 27.56)$ , all of these values are represented in table 3. Magnetic properties such as Bohr magnetic moments ( $\mu_B$ ), magneto crystalline anisotropy constant (K), starting permeability ( $\mu_i$ ), and synthesized samples were obtained using the following relationships [42].

$$\text{Bohr magneton } (\mu_B) = M \times M_s / 5585 \times \rho_{x\text{-ray}} \quad (10)$$

$$\text{Anisotropy constant (K)} = H_c \times M_s / 0.96 \quad (11)$$

$$\text{Initial permeability } (\mu_i) = M_s^2 \times D / K \quad (12)$$

where M, D, x, and B represent the molecular weight, crystallite size, GNP concentration, and experimental magnetic moment values of the synthetic sample, correspondingly.

Table 3 Magnetic parameters of *MCCDF-GNP* composites.

Sample ID	Magnetic moment ( $n_B$ )	Anisotropy constant K (erg/cm <sub>3</sub> )	Initial permeability ( $\mu_i$ )	Saturation magnetization $M_s$ (emu/g)
M1	0.7876	3637.70	68.52	95.00
M2	0.6846	4059.62	72.42	84.21
M3	0.6321	4295.01	51.99	75.99
M4	0.5283	2412.64	48.69	63.11
M5	0.4443	3011.69	27.56	52.52
M6	0.3568	1845.87	28.64	42.71

The ionic radii of doping concentration elements and other cations have a significant influence on the magnetic properties of spinel ferrites. As a result, the size of ionic radii and link lengths affect the magnetic behavior of nanoparticles [43][29]. For example, in the current *MCCDF-GNP* ferrite Composites, the ionic radii of  $\text{Cu}^{2+}$  ( $0.73 \text{ \AA}$ ),  $\text{Co}^{2+}$  ( $0.72 \text{ \AA}$ ),  $\text{Mg}^{2+}$  ( $0.65 \text{ \AA}$ ),  $\text{Dy}^{3+}$  ( $0.91 \text{ \AA}$ ), and  $\text{Fe}^{3+}$  ( $0.65 \text{ \AA}$ ). The magnetic moments of the substituents and other cations had a significant influence on the ferrite systems magnetic properties [44] [30].

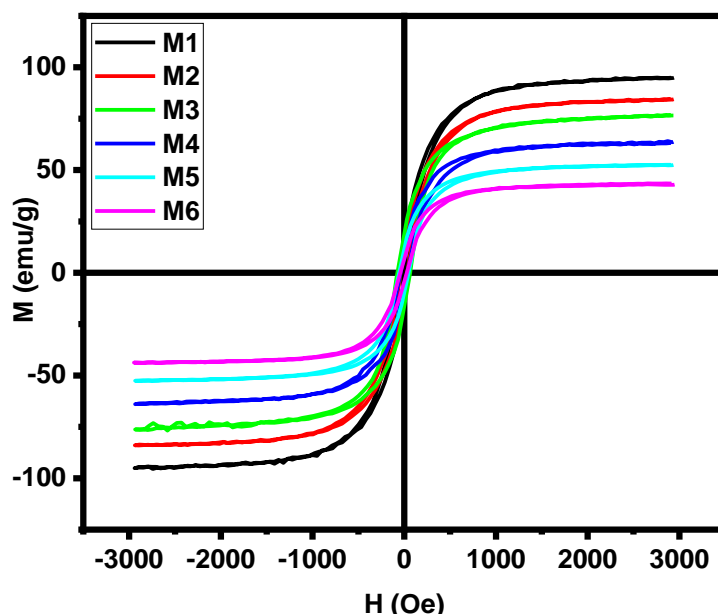


Fig. 7. *M-H loops of MCCDF-GNP Composites.*

#### 4. Conclusion

With the help of versatile sol-gel process MCCDF-GNP composites were successfully synthesized. The crystallites size was measured to be between 27.62 and 41.46 nanometers (nm) from XRD data. Composite materials have X-ray densities ranging from 4.68 - 4.88 g/cm<sup>3</sup>. The optical band gap was reduced from 3.50 to 2.88 eV as the Dy and GNP concentrations were increased. The resistivity decreased as the concentration of Dy and GNP rises. However, Raman spectra revealed five active modes in MCCDF-GNP Composites: A<sub>1g</sub>, E<sub>g</sub>, and T<sub>2g</sub>, indicating symmetric and anti-symmetric behavior of the vibrational band location. With increasing applied frequencies, the dielectric tangent loss for MCCDF-GNP Composites nanoparticles showed a significant diminishing trend. M-H hysteresis loop revealed that these composites exhibit ferromagnetic behavior, and the saturation magnetization decreases with increase of GNP in ferrite composites. This observation designated that these *MCCDF-GNP Composites* perform as a semiconductor property. These material can be utilized for humidity sensors, antenna, micro memory chips and catalytic activities.

#### Acknowledgements

Project supported by the Taif University Researchers Supporting project number (TURSP-2020/293), Taif University, Taif, Saudi Arabia.

#### References

- [1] Y. lei, Z. Yao, H. Lin, A. Ali Haidry, J. Zhou, P. Liu, Synthesis and high-performance microwave absorption of reduced graphene oxide/Co-doped ZnNi ferrite/polyaniline composites, *Mater. Lett.* **236**(1), 456 (2019). <https://doi.org/10.1016/j.matlet.2018.10.158>.
- [2] G. Zhang, R. Shu, Y. Xie, H. Xia, Y. Gan, J. Shi, J. He, Perrozzi, F., Prezioso, S., & Ottaviano, L. (2014). Graphene oxide: from fundamentals to applications. *Journal of Physics: Condensed Matter*, **27**(1), 209 (2018). <https://doi.org/10.1016/j.matlet.2018.08.055>.

- [3] S.C. Ray, Application and Uses of Graphene Oxide and Reduced Graphene Oxide, Elsevier Inc., 2015. <https://doi.org/10.1016/b978-0-323-37521-4.00002-9>.
- [4] Y.H. Ng, A. Iwase, N.J. Bell, A. Kudo, R. Amal, Semiconductor/reduced graphene oxide nanocomposites derived from photocatalytic reactions, *Catal. Today*. **164** (1), 353 (2011). <https://doi.org/10.1016/j.cattod.2010.10.090>.
- [5] E. Peng, E.S.G. Choo, P. Chandrasekharan, C.T. Yang, J. Ding, K.H. Chuang, J.M. Xue, Synthesis of manganese ferrite/graphene oxide nanocomposites for biomedical applications, *Small*. **8** (23), 3620 (2012). <https://doi.org/10.1002/sml.201201427>.
- [6] M.M.J. Sadiq, U.S. Shenoy, D.K. Bhat, Synthesis of BaWO<sub>4</sub>/NRGO-g-C<sub>3</sub>N<sub>4</sub> nanocomposites with excellent multifunctional catalytic performance via microwave approach, *Front. Mater. Sci.* **12** (8), 247 (2018). <https://doi.org/10.1007/s11706-018-0433-0>.
- [7] A.T. Smith, A.M. LaChance, S. Zeng, B. Liu, L. Sun, Synthesis, properties, and applications of graphene oxide/reduced graphene oxide and their nanocomposites, *Nano Mater. Sci.* **1**(1), 31 (2019). <https://doi.org/10.1007/s42452-021-04644-y>.
- [8] Z. Durmus, H. Kavas, A. Durmus, B. Aktaş, Synthesis and micro-structural characterization of graphene/strontium hexaferrite (SrFe<sub>12</sub>O<sub>19</sub>) nanocomposites, *Mater. Chem. Phys.* **163**(1), 439 (2015).
- [9] L. Thi Mong Thy, N. Hoan Kiem, T. Hoang Tu, L. Minh Phu, D. Thi Yen Oanh, H. Minh Nam, M. Thanh Phong, N.H. Hieu, Fabrication of manganese ferrite/graphene oxide nanocomposites for removal of nickel ions, methylene blue from water, *Chem. Phys.* **533**(1), 110700 (2020).
- [10] T. Imboon, J. Khumphon, K. Yotkuna, I.M. Tang, S. Thongmee, Enhancement of photocatalytic by Mn<sub>3</sub>O<sub>4</sub> spinel ferrite decorated graphene oxide nanocomposites, *SN Appl. Sci.* **3**(7), 22 (2021).
- [11] F. Paquin, J. Rivnay, A. Salleo, N. Stingelin, C. Silva, Multi-phase semicrystalline microstructures drive exciton dissociation in neat plastic semiconductors, *J. Mater. Chem. C*. **3**, 10715 (2015). <https://doi.org/10.1039/b000000x>.
- [12] Y. Ding, Q. Liao, S. Liu, H. Guo, Y. Sun, G. Zhang, Y. Zhang, Reduced Graphene Oxide Functionalized with Cobalt Ferrite Nanocomposites for Enhanced Efficient and Lightweight Electromagnetic Wave Absorption, *Sci. Rep.* **6**(87), 1 (2016). <https://doi.org/10.1038/srep32381>.
- [13] R. BoopathiRaja, M. Parthibavarman, A. Nishara Begum, Hydrothermal induced novel CuCo<sub>2</sub>O<sub>4</sub> electrode for high performance supercapacitor applications, *Vacuum*. **165**, 96 (2019). <https://doi.org/10.1016/j.vacuum.2019.04.013>.
- [14] P. Li, W. Sun, Q. Yu, P. Yang, J. Qiao, Z. Wang, D. Rooney, K. Sun, An effective three-dimensional ordered mesoporous CuCo<sub>2</sub>O<sub>4</sub> as electrocatalyst for Li-O<sub>2</sub> batteries, *Solid State Ionics*. **289**, 17 (2016). <https://doi.org/10.1016/j.ssi.2016.02.014>.
- [15] S. Ameer, I.H. Gul, M. Mujahid, Ultra low permittivity/loss CoFe<sub>2</sub>O<sub>4</sub> and CoFe<sub>2</sub>O<sub>4</sub>-rGO nanohybrids by novel 1-hexanol assisted solvothermal process, *J. Alloys Compd.* **642**(7), 78 (2015). <https://doi.org/10.1016/j.jallcom.2015.04.101>.
- [16] J.A. Vara, P.N. Dave, S. Chaturvedi, The catalytic investigation of nanoferrites on the thermal decomposition behavior of AN-based composite solid propellant, *Part. Sci. Technol.* **39**(17), 1 (2021). <https://doi.org/10.1080/02726351.2019.1639866>.
- [17] Z. Karimi, Y. Mohammadifar, H. Shokrollahi, S.K. Asl, G. Yousefi, L. Karimi, Magnetic and structural properties of nano sized Dy-doped cobalt ferrite synthesized by co-precipitation, *J. Magn. Magn. Mater.* **361**, 150 (2014). <https://doi.org/10.1016/j.jmmm.2014.01.016>.
- [18] R. Jain, V. Luthra, S. Gokhale, Dysprosium doping induced shape and magnetic anisotropy of Fe<sub>3-x</sub>Dy<sub>x</sub>O<sub>4</sub> (x=0.01-0.1) nanoparticles, *J. Magn. Magn. Mater.* **414**(15), 111 (2016). <https://doi.org/10.1016/j.jmmm.2016.04.069>.
- [19] S. Jauhar, J. Kaur, A. Goyal, S. Singhal, Tuning the properties of cobalt ferrite: A road towards diverse applications, 2016.
- [20] P. Maier, B. Clausius, J. Wicke, N. Hort, Characterization of an extruded Mg-Dy-Nd alloy during stress corrosion with C-ring tests, *Metals (Basel)*. **10**(11), 16 (2020).

- <https://doi.org/10.3390/met10050584>.
- [21] M. Verma, A.P. Singh, P. Sambyal, B.P. Singh, S.K. Dhawan, V. Choudhary, Barium ferrite decorated reduced graphene oxide nanocomposite for effective electromagnetic interference shielding, *Phys. Chem. Chem. Phys.* **17**(3), 1610 (2015).
- [22] I. Ahmed, G. Mustafa, M. Umair Subhani, G. Hussain, A.G. Ismail, H. Anwar, A detailed investigation of lanthanum substituted bismuth ferrite for enhanced structural, optical, dielectric, magnetic and ferroelectric properties, *Results Phys.* **38** 105584 (2022). <https://doi.org/10.1016/j.rinp.2022.105584>.
- [23] M. Nawaz, M.U. Islam, M.A. Nazir, I. Bano, I.H. Gul, M. Ajmal, Transport properties in spinel ferrite/graphene oxide nanocomposites for electromagnetic shielding, *Ceram. Int.* **47**(18), 25505 (2021).
- [24] C. Lin, M.L. Povinelli, Optical absorption enhancement in silicon nanowire arrays with a large lattice constant for photovoltaic applications, *Opt. Express.* **17**(22), 19371 (2009). <https://doi.org/10.1364/oe.17.019371>.
- [25] Y. Köseoğlu, M.I. Oleiwi Oleiwi, R. Yilgin, A.N. Koçbay, Effect of chromium addition on the structural, morphological and magnetic properties of nano-crystalline cobalt ferrite system, *Ceram. Int.* **38**(8), 6671 (2012). <https://doi.org/10.1016/j.ceramint.2012.05.055>.
- [26] Massoudi, M. Smari, K. Nouri, E. Dhahri, K. Khirouni, S. Bertaina, L. Bessais, E.K. Hlil, Magnetic and spectroscopic properties of Ni-Zn-Al ferrite spinel: From the nanoscale to microscale, *RSC Adv.* **10**, 34556–34580 (2020). <https://doi.org/10.1039/d0ra05522k>.
- [27] K. Hussain, N. Amin, M.I. Arshad, Evaluation of structural, optical, dielectric, electrical, and magnetic properties of Ce<sup>3+</sup> doped Cu<sub>0.5</sub>Cd<sub>0.25</sub>Co<sub>0.25</sub>Fe<sub>2-x</sub>O<sub>4</sub> spinel nano-ferrites, *Ceram. Int.* **47**(18), 3401–3410 (2021).
- [28] G. Hussain, I. Ahmed, A.U. Rehman, M.U. Subhani, N. Morley, M. Akhtar, M.I. Arshad, H. Anwar, Study of the role of dysprosium substitution in tuning structural, optical, electrical, dielectric, ferroelectric, and magnetic properties of bismuth ferrite multiferroic, *J. Alloys Compd.* **919** 165743(2022). <https://doi.org/10.1016/j.jallcom.2022.165743>.
- [31] Y. Tian, Z. Yu, L. Cao, X.L. Zhang, C. Sun, D.W. Wang, Graphene oxide: An emerging electromaterial for energy storage and conversion, *J. Energy Chem.* **55**(47), 323 (2021). <https://doi.org/10.1016/j.jechem.2020.07.006>.
- [32] M. Saleem, D. Varshney, Effect of chromium doping on the structural and vibrational properties of Mn-Zn ferrites, *AIP Conf. Proc.* **1953**(8), 5 (2018). <https://doi.org/10.1063/1.5032428>.
- [33] E.E. Ateia, A.T. Mohamed, K. Elsayed, Impact of Gd<sup>3+</sup>/graphene substitution on the physical properties of magnesium ferrite nanocomposites, *J. Magn. Magn. Mater.* **452**(15), 169 (2018). <https://doi.org/10.1016/j.jmmm.2017.12.053>.
- [34] A.L. Patterson, The scherrer formula for X-ray particle size determination, *Phys. Rev.* **56**(15), 978 (1939). <https://doi.org/10.1103/PhysRev.56.978>.
- [35] M. Ajmal, M.U. Islam, A. Ali, Structural, Electrical and Dielectric Properties of Hexa-ferrite-Polyaniline Nano-composites, *J. Supercond. Nov. Magn.* **31**(12) 1375 (2018). <https://doi.org/10.1007/s10948-017-4332-x>.
- [36] K. Hussain, A. Bibi, F. Jabeen, N. Amin, K. Mahmood, A. Ali, M.Z. Iqbal, M.I. Arshad, Study of structural, optical, electrical and magnetic properties of Cu<sup>2+</sup>-doped Zn<sub>0.4</sub>Co<sub>0.6-x</sub>Ce<sub>0.1</sub>Fe<sub>1.9</sub>O<sub>4</sub> spinel ferrites, *Phys. B Condens. Matter.* **584**(1), 412078 (2020). <https://doi.org/10.1016/j.physb.2020.412078>.
- [37] R.A. Pawar, S.M. Patange, Q.Y. Tamboli, V. Ramanathan, S.E. Shirsath, Spectroscopic, elastic and dielectric properties of Ho<sup>3+</sup> substituted Co-Zn ferrites synthesized by sol-gel method, *Ceram. Int.* **42**(14), 16096 (2016).
- [38] B.S. Holinsworth, D. Mazumdar, H. Sims, Q.C. Sun, M.K. Yurtisigi, S.K. Sarker, A. Gupta, W.H. Butler, J.L. Musfeldt, Chemical tuning of the optical band gap in spinel ferrites: CoFe<sub>2</sub>O<sub>4</sub> vs NiFe<sub>2</sub>O<sub>4</sub>, *Appl. Phys. Lett.* **103**(31), 2 (2013).
- [39] J. Chen, W. Wang, M.A. Reed, A.M. Rawlett, D.W. Price, J.M. Tour, Room temperature negative differential resistance in nanoscale molecular junctions, *Mater. Res. Soc. Symp. - Proc.* **582**(16), H321 (2001). <https://doi.org/10.1063/1.1289650>.
- [40] C. V. Ramana, Y.D. Kolekar, K. Kamala Bharathi, B. Sinha, K. Ghosh, Correlation

- between structural, magnetic, and dielectric properties of manganese substituted cobalt ferrite, *J. Appl. Phys.* **114**(18), 348 (2013).
- [41] A. Aslam, A.U. Rehman, N. Amin, M. Ajaz un Nabi, Q. ul ain Abdullah, N.A. Morley, M.I. Arshad, H.T. Ali, M. Yusuf, Z. Latif, K. Mehmood, Lanthanum doped  $Zn_{0.5}Co_{0.5}La_xFe_{2-x}O_4$  spinel ferrites synthesized via co-precipitation route to evaluate structural, vibrational, electrical, optical, dielectric, and thermoelectric properties, *J. Phys. Chem. Solids.* **154** 110080 (2021).
- [42] D. Ravinder, P. Vijaya Bhasker Reddy, High-frequency dielectric behaviour of Li-Mg ferrites, *Mater. Lett.* **57**(26), 4344 (2003). [https://doi.org/10.1016/S0167-577X\(03\)00093-4](https://doi.org/10.1016/S0167-577X(03)00093-4).
- [43] A. Kumar, P. Sharma, D. Varshney, Structural, vibrational and dielectric study of Ni doped spinel Co ferrites:  $Co_{1-x}Ni_xFe_2O_4$  ( $x=0.0, 0.5, 1.0$ ), *Ceram. Int.* **40**(8), 12855 (2014). <https://doi.org/10.1016/j.ceramint.2014.04.140>.
- [44] S. Jandl, J. Deslandes, Infrared spectra of  $HfS_3$ , *Phys. Rev. B.* **24**(25), 1040 (1981).